JOURNAL OF AIRCRAFT
Vol. 48, No. 4, July–August 2011

Ionospheric Threat Mitigation by Geometry Screening in Ground-Based Augmentation Systems

Jiyun Lee*
Korea Advanced Institute of Science and Technology, Daejeon 305-701, Republic of Korea
and
Jiwon Seo,† Young Shin Park,‡ Sam Pullen,§ and Per Enge¶
Stanford University, Stanford, California 94305

DOI: 10.2514/1.C031309

Large spatial variations in ionospheric delay of Global Navigation Satellite System signals observed during severe ionospheric storms pose potential threats to the integrity of the Ground-Based Augmentation System, which supports aircraft precision approaches and landing. Range-domain monitoring within the Ground-Based Augmentation System ground facility cannot completely eliminate all possible ionospheric threats, because ionospheric gradients are not observable to the ground monitor if they impact the satellite-to-ground lines of sight with the worst-possible geometry and velocity. This paper proposes an algorithm called *position-domain geometry screening* to remove potentially hazardous satellite geometries under worst-case ionospheric conditions. This is done by inflating one or more integrity parameters broadcast by the ground facility. Hence, the integrity of the system can be guaranteed without any modification of existing avionics. This paper develops an algorithm that allows the ground station to conservatively estimate the worst-case ionospheric errors for Ground-Based Augmentation System users. The results of this algorithm determine which potential aircraft satellite geometries are safe and which are unsafe, and inflation of the broadcast σ_{vig} parameter is used to make all unsafe geometries unusable for the Ground-Based Augmentation System. Although the elimination of unsafe geometries reduces system availability, this paper shows that acceptable availability for category I precision approaches is attainable at Memphis International Airport and Newark Liberty International Airport while guaranteeing system integrity under anomalous ionospheric gradients.

I. Introduction

THE Ground-Based Augmentation System (GBAS) (known as the Local Area Augmentation System, or LAAS, in the United States [1]) is designed to augment Global Navigation Satellite Systems (GNSS) (e.g., the Global Positioning System, or GPS, in the United States and Galileo in Europe [2,3]) to enable GNSS-based aircraft landing guidance. A GBAS ground facility is fielded within the property of a particular airport as illustrated in Fig. 1. It measures and monitors GNSS signals and broadcasts pseudorange differential corrections and integrity information for satellites via a very-high-frequency (VHF) data broadcast transmitter. This information allows GBAS-equipped receivers on aircraft near the airport to compute the error bounds of its position solution with extremely high confidence and thus verify the safety of approach and landing operations in real time.

Almost all anomalies that could pose a threat to GBAS-supported approach and landing can be detected by monitoring of pseudorange measurements (in short, range-domain monitoring) performed by the GBAS ground facility. However, extremely large spatial gradients of GNSS signal delay due to anomalous ionospheric conditions pose a potential threat to the integrity of the guidance system. Since GBAS reference receivers provide range-domain corrections for GNSS satellite measurements to airborne receivers within 45 km, significant ionospheric delay variation over short separations can cause nonnegligible user errors. For reasons that will be explained later, this threat cannot be completely mitigated by range-domain monitoring alone.

Datta-Barua et al. [4] first investigated anomalous ionospheric gradients discovered in 2000 by the new Wide Area Augmentation System (WAAS) [5] network of GPS reference receivers and discovered gradients as large as hundreds of mm/km (or hundreds of parts per million), which is far larger than typical ionospheric gradients of 1–5 mm/km. Even larger gradients were observed during the very powerful ionospheric storms of October and November 2003 [6,7]. Although gradients of hundreds of mm/km are very rare, the magnitude of potential GBAS user errors due to them exceeds what can be practically detected or bounded in range-domain.

To parameterize the potential threat due to ionospheric anomalies, extensive data analysis including all available ionospheric storm data in the conterminous U.S. (CONUS) was performed [6,7]. Based on the parameterized threat space, a novel position-domain mitigation technique has been developed. This method was designed to support the airborne receiver standards for category I precision-approach operations that had already been developed [8]. Subsequently, Mayer et al. [9] developed a less-threatening ionosphere threat space for Germany based on data collected there, but the CONUS threat model is used exclusively in this paper.

This paper describes a position-domain verification methodology known as geometry screening that was originally developed by the authors [10] and has been implemented by the Honeywell SLS-4000 category I LAAS ground facility to mitigate ionospheric threats in CONUS [11]. (Refer to [12] for a position-domain monitor for detecting mismodeling of GBAS tail error distributions, which is different from the geometry screening proposed in this paper for mitigating ionospheric threats.) Integrity information broadcast from the ground facility is adjusted by the mitigation algorithm so that potentially hazardous satellite geometries under ionospheric anomalies cannot be used by GBAS avionics. More recently, a simpler method of geometry screening within GBAS avionics has been

Received 11 November 2010; revision received 18 February 2011; accepted for publication 22 February 2011.

*Assistant Professor, Department of Aerospace Engineering, 335 Gwahangno, Yuseong-gu; jiyunlee@kaist.ac.kr.

†Postdoctoral Scholar, Department of Aeronautics and Astronautics, 496 Lomita Mall; jwseo@cs.stanford.edu (Corresponding Author).

‡Research Assistant, Department of Aeronautics and Astronautics, 496 Lomita Mall.

§Senior Research Engineer, Department of Aeronautics and Astronautics, 496 Lomita Mall.

¶Professor, Department of Aeronautics and Astronautics, 496 Lomita Mall. Member AIAA.

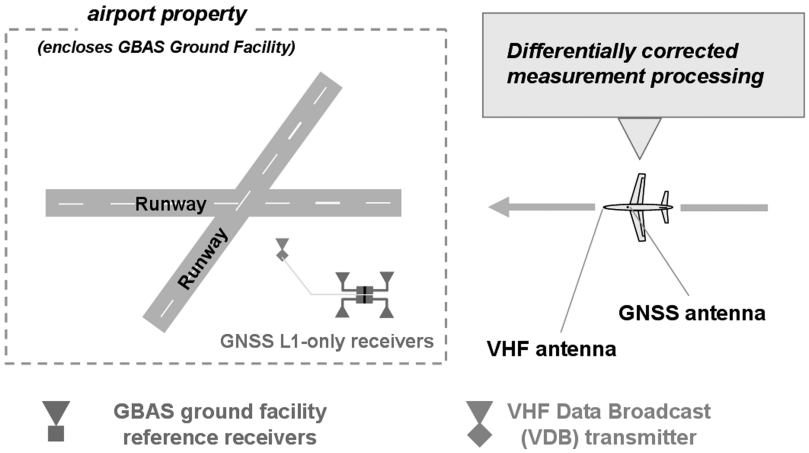

Fig. 1 Illustration of a typical GBAS configuration.

proposed for the GAST-D version of GBAS that will support categories II and III approaches for properly equipped users [13]. A major advantage of screening at the aircraft is that the actual satellite geometry is known, whereas the ground-based method described in this paper requires the evaluation of many possible airborne satellite geometries. However, applying geometry screening only at the aircraft requires additional ionospheric monitoring in both the ground station and aircraft that has not yet been fully validated.

After describing the threat posed by the anomalous gradient and developing an ionospheric threat model for CONUS in Sec. II, we provide a detailed study of GBAS errors induced by ionospheric anomalies in the range and position domains in Sec. III. Section IV develops the position-domain geometry-screening method that mitigates this threat. Further, a new mathematical expression to calculate ionosphere-induced vertical position errors is suggested. Although geometry screening involves increasing position bounds and therefore lowering availability, the simulation results in Sec. IV demonstrate that this method provides acceptable availability for category I GBAS operations at Memphis International Airport and Newark Liberty International Airport. Section V describes how geometry screening is implemented in real time in GBAS ground stations. Our conclusions are given in Sec. VI.

II. Ionospheric Gradient and Threat Model

A. Nominal and Anomalous Ionospheric Gradients

Among the various GNSS error sources, error introduced by the ionosphere is one of the largest and most variable for single-frequency GNSS users. The ionosphere is an ionized plasma region located in the Earth's upper atmosphere from about 50–2000 km in altitude. Because of the free electrons and ions produced by solar radiation, radio signals are refracted as they propagate through this region. The main effect of this refraction is a delay in the code-phase measurement of GNSS signals and an advance in the carrier-phase measurement by an equal amount. This divergence of code and carrier measurements, usually called code–carrier divergence (CCD), is one method that is used to detect anomalous ionospheric behavior (details will be provided in Sec. III.A).

Under nominal conditions (without ionospheric storms), ionospheric delays on GPS pseudorange measurements are very highly correlated over the short separations between a GBAS ground facility and approaching airplanes. Thus, differential GBAS user errors caused by typical ionospheric delays are very small and do not measurably affect system performance. However, unusual solar events such as coronal mass ejections can cause the ionosphere to behave very differently. Extremely large ionospheric gradients observed during past severe ionospheric storms produced spatial gradients that were two orders of magnitude higher than the standard broadcast 1σ value of 4 mm/km, which was chosen as a conservative bound on nominal zenith ionospheric spatial gradients [14]. Gradients this large, if undetected, could generate vertical position errors significantly exceeding the tolerable error limit, which will be explained with details in Sec. III.B.

As mentioned earlier, Datta-Barua et al. [4] first analyzed WAAS [5] data during the 6–7 April 2000 ionospheric storms and observed gradients as large as 320 mm/km in slant (along the actual path between a satellite and a receiver). The discovery of gradients of this magnitude was a major surprise to the GBAS community because they could not be bounded by the broadcast ionospheric σ. Before investigating possible mitigation techniques, the ionospheric threat caused by large spatial gradients needed to be better-understood and parameterized based on previous observations. The ionospheric threat model in CONUS, which has been developed from several years' effort of multiple researchers, is introduced in the next section.

B. Ionospheric Threat Model for CONUS

The simplified ionospheric front geometry shown in Fig. 2 was used to develop the CONUS ionospheric threat model [6]. This model assumes a linear, semi-infinite ionospheric front that moves with constant speed relative to the ground. The threat model is parameterized by the spatial gradient (or slope) in slant ionospheric delay, the width of the zone where the gradient is present (i.e., the distance between low and high-delay regions), and the propagation speed of an ionospheric front. Note that the product of width and gradient yields a total difference in slant ionospheric delay. Each of these parameters is bounded in the ionospheric anomaly threat space summarized in Table 1. The upper bound on the gradient is given as a

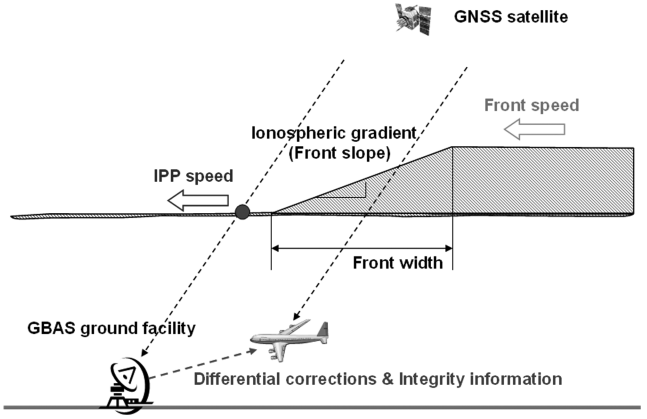

Fig. 2 Illustration of ionospheric front model. The range delay suffered at the ground facility is significantly different from the delay suffered by the aircraft in this scenario. If the front speed matches or lines up with the IPP speed, the large ionospheric gradient is not observable to the ground monitor. This undetected postcorrection range error is potentially hazardous.

Table 1 Ionospheric gradient threat space

Parameter	Value
Max. front slope, mm/km	
Low elevation (<15°)	375
Medium elevation (15° < El < 65°)	375 + 50(El − 15)/50
High elevation (>65°)	425
Front width, km	25–200
Front speed, m/s	0–750
Max. differential delay, m	50

function of satellite elevation angle: 375 mm/km at low elevation (below 15 deg), increasing linearly to 425 mm/km at high elevation (above 65 deg). These bounds slightly exceed the largest gradient validated from the CONUS data analysis due to margin added to account for measurement and estimation errors. In addition to the maximum gradient bounds, bounds were established on ionospheric front speed with respect to the ground (up to 750 m/s), ionospheric front width (between 25 and 200 km), and total differential delay (up to 50 m) [6,7]. The limit on the total delay difference acts as a constraint on the allowed combinations of width and gradient. For example, 350 mm/km and 200 km both fall within the limits for gradient and width, respectively, but their product is an implied total differential delay of 70 m, which exceeds the 50 m limit. Therefore, this combination of gradient and width falls outside the threat model.

Note that this threat model only describes potential ionospheric behavior and thus does not include other parameters that are necessary for analyzing anomalous-ionosphere-induced errors on GBAS avionics. These additional factors include the orientation of an ionospheric front with respect to an approaching airplane and a runway, the horizontal-approach speed of the aircraft, and the velocities of the ionospheric pierce points (IPPs), which represent the theoretical intersections between lines of sight to satellites and the ionosphere when modeled as a thin shell at a particular altitude above the Earth (typically 350–450 km). Figure 2 illustrates a possible configuration of an ionospheric front, airplane, runway, GBAS ground facility, and GNSS satellite. If the front velocity and the IPP velocity are the same (or very close) in direction and magnitude, the ionospheric delay observed by the ground facility does not change in time fast enough to be detected by the CCD monitor; hence, the anomalous gradient is not observable to a category I ground facility (a detailed explanation of the worst-case geometry with two impacted satellites is given in Sec. III.A). GAST-D ground facilities plan to add differential smoothed-code or carrier monitors over medium-to-long baselines to make large gradients observable directly, without requiring a significant change over time [15].

In Fig. 2, the ionospheric delay suffered at the ground facility is significantly different from the delay suffered by the aircraft. Hence, large range errors would remain even after the aircraft applies differential corrections to its range measurements. If these errors grow large enough before detection, they can cause an integrity risk to the affected aircraft.

III. Ionosphere-Induced Errors Because of Anomalous Ionospheric Gradients

This section describes in detail how anomalous ionospheric gradients can induce undetected errors in the range and position domain. Closed-form equations modeling the magnitude of range-domain errors are introduced. It is also explained that the protection level (the confidence bound on position solutions) calculated by airborne users with the nominal range-error bounds broadcast by the GBAS ground facility may not prevent integrity risk under severe ionospheric storm conditions. As noted above, this is because CCD monitors within the ground facility cannot detect anomalous ionospheric gradients with a specific geometry of satellites and ionospheric front movement.

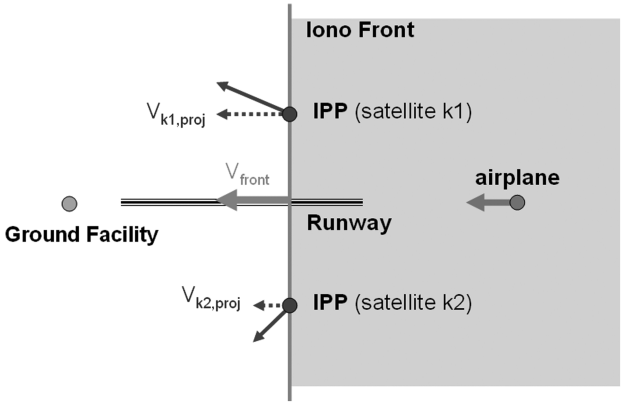

Fig. 3 An example worst-case geometry causing undetected range errors. If the projected velocity of satellite *k*1 matches with the velocity of the ionospheric front moving to the runway direction, the CCD monitor within the ground facility cannot detect the anomalous gradient impacting satellite *k*1.

A. Ionosphere-Induced Errors in the Range Domain

The CCD monitor within the GBAS ground facility is present to detect satellite-generated divergence but can also be used to detect anomalous ionospheric conditions [16]. Since the CCD monitor observes the time-variation of divergence between code and carrier measurements caused by dispersive media such as the ionosphere, its detection capability depends on the relative speed of an ionospheric front with respect to the lines of sight from the ground facility to satellites. Figure 3 illustrates an example worst-case scenario of ionospheric front movement, runway direction, and movement of ionospheric pierce points (IPPs) between the ground facility and two satellites. Under this scenario, the ionospheric front moves in the same direction as an aircraft performing a straight-in runway approach and impacts the IPPs of two satellites (satellites $k1$ and $k2$ in Fig. 3) simultaneously. At the same time, the velocity of one satellite projected onto the line perpendicular to the front ($V_{k1,\text{proj}}$) happens to be the same as the velocity of the ionospheric front (V_{front}).

As mentioned earlier, the detection capability of the CCD monitor depends on a relative speed, Δv, between the ionospheric front and the projected IPP velocity. Hence, if $V_{k1,\text{proj}}$ is the same as V_{front} as shown in Fig. 3, $\Delta v = |V_{k1,\text{proj}} - V_{\text{front}}| = 0$; the ionospheric gradient is not observable by the CCD monitor. Consequently, the remaining error on the airborne ranging measurement of satellite $k1$ can grow large without a timely alert, which implies an integrity risk. Therefore, the CCD monitor alone cannot prevent the potential integrity failure caused by ionospheric anomalies under specific worst-case combinations of geometries.

At a given epoch, the IPP velocities of the satellites in view are generally different. If the IPP of one satellite has zero Δv (as for the case of satellite $k1$ in Fig. 3), the IPP of the other satellite (i.e., satellite $k2$) at the same epoch generally has nonzero Δv (i.e., $\Delta v = |V_{k2,\text{proj}} - V_{\text{front}}| \neq 0$). Hence, there is a higher chance for an anomalous ionospheric gradient impacting the IPP of satellite $k2$ to be detected by the CCD monitor. Based on this concept and a mathematical model of the CCD monitor, Ramakrishnan et al. [17] presented closed-form expressions for ionosphere-induced range errors as functions of the relative speed Δv, based on the model originally suggested by P. Enge.** These expressions have been updated and used in [18,19] and can be summarized as follows (the derivation of these models is beyond the scope of this paper).

When Δv is small, a category I ground station that is reliant on the CCD monitor cannot detect anomalous ionospheric gradients, as explained above. Hence, to guarantee aviation integrity with a minimum reliance on assumptions, it is assumed that an undetected anomalous gradient always exists in this case. If the undetected anomalous gradient occurs with the worst-case geometry, ionosphere-induced range errors increase as the effective separation between the

**Private communication, P. Enge, May 2007.

GBAS ground facility and an approaching airplane increases, and this increase happens within the region of the linear change in slant ionospheric delay defined with the front width in Fig. 2. The effective separation includes a physical separation, x_{aircraft}, between ground facility and airplane and a synthetic separation, $2\tau v_{\text{aircraft}}$, due to the memory of the single-frequency carrier-smoothing filter in both ground and airborne GBAS measurement processing [16]. The maximum ionospheric gradient g is obtained from the CONUS ionospheric threat model [6] as a function of satellite elevation. Since the maximum differential slant delay is 50 m from the threat model, a gradient g greater than $50/w$ is not valid under the threat model and is discarded from ionosphere-induced range-error calculations (w is the ionospheric front width as defined in Fig. 2). As a result, the closed-form approximation of the ionosphere-induced differential range error ε for small Δv is expressed as follows:

$$\varepsilon = \min\left(\frac{50}{w}, g\right) \times (x_{\text{aircraft}} + 2\tau v_{\text{aircraft}}) \quad \text{if } \Delta v < \frac{0.0229}{\min(\frac{50}{w}, g)} \quad \text{and} \quad \Delta v < 0.11 \tag{1}$$

where ε is the ionosphere-induced differential range error (meters); w is the ionospheric front width (kilometers) (refer to Fig. 2); g is the ionospheric gradient (m/km) (refer to Fig. 2); x_{aircraft} is the physical separation between the GBAS ground facility and an approaching airplane (kilometers); τ is the time constant of the single-frequency GBAS carrier-smoothing filter, 100 s for category I GBAS; v_{aircraft} is the velocity of an approaching airplane (km/s) (this paper assumes a constant velocity of 0.07 km/s); Δv is the relative speed between the ionospheric front velocity and the projected velocity of an IPP (km/s) (refer to Fig. 3). The constants 0.0229 and 0.11, specifying the boundary of a small Δv, are obtained from the CONUS threat model [6] and a conservative mathematical model of the minimum detectable error of the ground-station CCD monitor [16,19].

When Δv is moderate, the CCD monitor can detect some anomalous gradients before the maximum differential error occurs. Under the CONUS threat model, ionosphere-induced differential range errors grow no greater than 4 m in this case [17]. Hence, the closed-form model of the ionosphere-induced differential range error ε for a moderate Δv is

$$\varepsilon = 4, \quad \text{if } \frac{0.0229}{\min(\frac{50}{w}, g)} < \Delta v < 0.11 \tag{2}$$

When Δv is large, the anomalous gradients are detected by the CCD monitor with a very small probability of missed detection. Under the CONUS threat model, ionosphere-induced differential range errors grow no greater than 2.5 m in this case [17]. Hence, the closed-form model is

$$\varepsilon = 2.5, \quad \text{if } \Delta v > 0.11 \tag{3}$$

Once the satellite geometry at a particular GBAS location is known from an almanac, we can hypothesize the worst-case geometry of Fig. 3 for each individual satellite and pair of satellites with known IPP velocities at each epoch. The paired-satellite scenario always assumes that the velocity of one satellite (satellite $k1$ in Fig. 3) projected onto the line perpendicular to the ionospheric front is the same as the velocity of the front (this is the same assumption that would be made for the case where satellite $k1$ is the only satellite impacted). Thus, Δv of the other satellite (satellite $k2$) in the paired case is obtainable from the satellite geometry alone; Δv of satellite $k2$ is the same as the relative projected velocity of satellite $k2$ with respect to the projected velocity of satellite $k1$. Therefore, an almanac and the ionospheric threat model (i.e., the range of possible front widths, gradients, and velocities) provide enough information to study ionosphere-induced differential range errors using Eqs. (1–3).

For this model, the worst-case ionosphere-induced error in both the range and position domains is given by the worst pair of satellites. It is theoretically possible for three or more satellites to be simultaneously impacted by the same ionospheric front, but such scenarios are both very improbable and are generally no more threatening to precision-approach operations than the worst two-satellite case. This is because as more satellites are impacted by the ionospheric front, a significant fraction of the induced error becomes common mode, and this component of the error only affects the GBAS clock solution.

B. Ionosphere-Induced Errors in the Position Domain

The closed-form expressions of ionosphere-induced differential range errors under the CONUS ionospheric threat model were introduced in Sec. III.A. Using these range-error models, ionosphere-induced errors in the position domain are examined in this section. Specifically, we are interested in the largest possible vertical position errors resulting from the range errors of the worst-case geometries at each epoch, as this is directly related to the integrity of GBAS systems (undetected errors exceeding a safe error limit are threatening to the users). Figure 3 shows an example worst-case geometry that results in ionosphere-induced errors without being detected by the CCD monitor. Because the CCD monitor may not alert such errors, this worst-case situation must always be assumed in order to guarantee aviation integrity without relying on the rarity of the underlying event. The ionosphere-induced vertical position error (denoted as ionosphere-induced error in vertical, or IEV) for a satellite pair ($k1$, $k2$) can be obtained from Eq. (4):

$$\begin{gathered}
\text{IEV}_{k1,k2} = |S_{\text{vert},k1}\varepsilon_{k1}| + |S_{\text{vert},k2}\varepsilon_{k2}| \\
S \equiv (G^T W G)^{-1} G^T W \\
G_i = [-\cos\text{El}_i \cos\text{Az}_i \quad -\cos\text{El}_i \sin\text{Az}_i \quad -\sin\text{El}_i \quad 1] \\
W^{-1} = \begin{bmatrix} \sigma_1^2 & 0 & \dots & 0 \\ 0 & \sigma_1^2 & \dots & 0 \\ \vdots & \vdots & \ddots & \vdots \\ 0 & 0 & \dots & \sigma_N^2 \end{bmatrix}
\end{gathered} \tag{4}$$

where $S_{\text{vert},ki}$ is the vertical position component of the weighted-least-squares projection matrix S for satellite ki (refer to Sec. 2.3.10.2 in [8]), $S_{\text{vert},ki}$ is dependent on the satellite geometry (the number and geometric distribution of satellites in view) at each epoch, ε_{ki} is the ionosphere-induced range error for satellite ki, G_i is the ith row of the observation matrix G, corresponding to the ith satellite in view (satellite i, for simplicity); El_i is the elevation of satellite i; Az_i is the azimuth of satellite i; W^{-1} is the inverse of the least squares weighting matrix; and σ_i^2 is the variance of a normal distribution that overbounds the true postcorrection range-domain error distribution for satellite i under the fault-free hypothesis.

The range errors ε in Eqs. (1–3) are absolute values of actual range errors. Theoretically, the range errors of the two satellites in Fig. 3 can have any combination of positive or negative signs. The absolute value of each term is taken in Eq. (4), which results in the largest possible bounding IEV for any possible combination of signs of range errors on two impacted satellites. (Note that $S_{\text{vert},ki}$ can also be positive or negative, but it is determined by the satellite geometry regardless of ionospheric front configuration.)

For a given satellite pair, the ionospheric front velocity is always assumed to match the projected velocity of one satellite (i.e., either $V_{\text{front}} = V_{k1,\text{proj}}$, as in Fig. 3, or $V_{\text{front}} = V_{k2,\text{proj}}$). After calculating IEVs for both cases, the greater IEV value is selected because we are interested in the worst-possible vertical position error at each epoch. Note that any satellite pair from all satellites in view can be potentially impacted by the ionospheric front. Hence, the IEVs of every satellite pair from an approved satellite geometry that can be used by an approaching airplane should be calculated and compared in order to obtain the maximum IEV (MIEV) for that particular geometry. If there are k satellites in view, for example, the IEVs of

$$\binom{k}{2}$$

possible satellite pairs are calculated and compared in order to obtain MIEV.

For various reasons, satellites that are visible to the GBAS ground facility may not be included in the positioning solution of an approaching airplane. To represent this possibility, it is assumed that up to two satellites from the all-in-view satellite set at the ground facility are not used by airborne GBAS avionics during the final-approach segment. Hence, if there are N satellites visible to the GBAS ground facility, there are

$$\sum_{k=N-2}^{N}\binom{N}{k}$$

subset satellite geometries (subsets of the set of satellites visible to the GBAS ground facility), which can be possibly used by the airplane. Note that each subset geometry has its own MIEV; thus the maximum over all possible subsets (including the all-in-view geometry) for a particular epoch can be thought of as the maximum MIEV for that epoch. However, the maximum MIEV has little practical significance, as *every* MIEV that exceeds the tolerable limit must be mitigated, not just the worst one.

Figure 4 shows an example of MIEV values for a particular epoch. Since there are seven satellites in view at this epoch, the total number of subset geometries to consider is

$$\sum_{k=5}^{7}\binom{7}{k}$$

Each of these subset geometries is represented with an index number (in no particular order) on the x axis of Fig. 4, and the MIEV of each subset geometry is plotted on the y axis. The MIEVs of 11 geometries are greater than the category I tolerable error limit (TEL) in the vertical direction (28.78 m at the minimum decision height of 200 ft) derived from the obstacle clearance surface for precision approach [20]. The geometries with indices of 4 and 25 have MIEVs greater than 50 m. These (hypothetical) large vertical position errors exceeding TEL are not acceptable for GNSS-based aircraft landing systems. Although some of the potentially hazardous geometries with MIEVs exceeding TEL are excluded by the nominal operation of airborne GBAS avionics, which will be explained in the next subsection, all must be excluded to mitigate the potential integrity risk.

C. Range-Domain Error Bounds and Protection Levels

An airborne GBAS receiver calculates the confidence bound of its position solution (usually called its *protection level*) at each epoch based on the satellite geometry and the broadcast range-domain σ (standard deviations of zero-mean Gaussian distributions that overbound the true signal-in-space error distributions) from the ground facility. The vertical protection levels (VPLs) are calculated at each epoch using Eqs. (5) and (6) (see Secs. 2.3.11.5.2.1.4 and 2.3.11.5.2.1.5 in [8]; note that VPL_{H1} is not shown here because it is not relevant to ionospheric geometry screening):

$$\mathrm{VPL}_{H0} = K_{\mathrm{ffmd}}\sqrt{\sum_{i=1}^{N} S_{\mathrm{vert},i}^2\sigma_i^2} \tag{5}$$

$$\mathrm{VPL}_{\mathrm{eph}} = \max_k(\mathrm{VPL}_{\mathrm{eph},k})$$

$$\mathrm{VPL}_{\mathrm{eph},k} = |S_{\mathrm{vert},k}|x_{\mathrm{aircraft}}P_k + K_{\mathrm{md\_eph}}\sqrt{\sum_{i=1}^{N} S_{\mathrm{vert},i}^2\sigma_i^2\Delta} \tag{6}$$

where VPL_{H0} is the vertical protection level (bound on vertical position error) under the fault-free hypothesis, K_{ffmd} is the multiplier (unitless), which determines the probability of fault-free missed detection, $K_{\mathrm{ffmd}} = 5.847$ for four ground subsystem reference antennas to provide the required probability of 10^{-7} (refer to Sec. 2.3.11.5.2.1.4 in [8]), $S_{\mathrm{vert},i}$ is the vertical position component of the weighted-least-squares projection matrix for satellite i, σ_i^2 is the variance of a zero-mean Gaussian distribution that overbounds the true range-domain postcorrection error distribution for satellite i under the fault-free hypothesis, $\mathrm{VPL}_{\mathrm{eph},k}$ is the vertical protection level under a single-satellite (satellite k) ephemeris fault, x_{aircraft} is the physical separation between the GBAS ground facility and the approaching airplane, P_k is the ephemeris error decorrelation parameter for satellite k [$P_k = 0.00018$ is used in this paper (refer to [18,19])], and $K_{\mathrm{md\_eph}}$ is the multiplier (unitless) derived from the probability of missed detection given that there is an ephemeris error in a GPS satellite [$K_{\mathrm{md\_eph}} = 5.085$ is used in this work (refer to [18,19])].

Figure 5 shows an example of calculated VPLs at the same epoch as Fig. 4. The VPL in Fig. 5 for each subset geometry is obtained as the larger value between two vertical position bounds, VPL_{H0} in Eq. (5) and $\mathrm{VPL}_{\mathrm{eph}}$ in Eq. (6). If the VPL of a certain geometry exceeds the 10 m vertical alert limit (VAL) for category I precision approach, the geometry is not approved for use. Hence, the geometries with indices 4, 17, and 25 in Fig. 5 are not approved and will not be used by an airplane. If an airplane views one of these unapproved geometries with VPLs exceeding VAL at this epoch, onboard

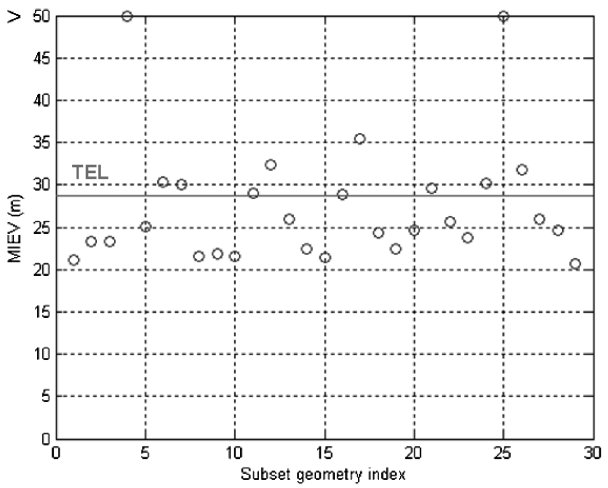

Fig. 4 MIEV of each subset geometry. Given seven satellites in view at this epoch, 29 possible subset geometries can be used by an approaching airplane. The 11 subset geometries with MIEVs exceeding the TEL are potentially hazardous for aircraft landing guidance.

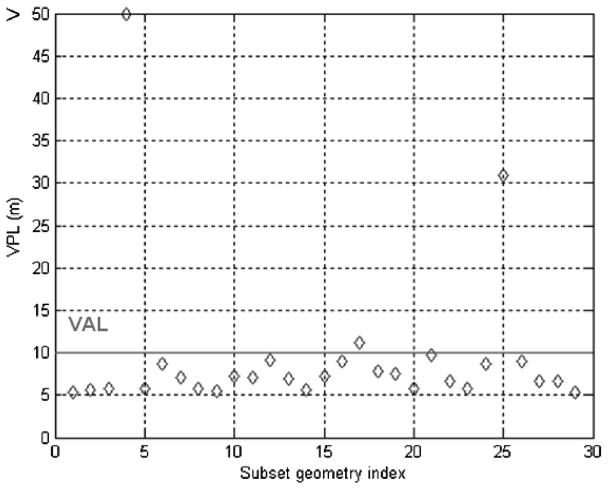

Fig. 5 VPLs with nominal range-domain error bounds at the same epoch as Fig. 4. The subset geometries with VPLs exceeding the VAL are not approved for positioning. Hence, they cannot cause an integrity failure even though their MIEVs are greater than the tolerable error limit in Fig. 4.

avionics raise a flag and hence a pilot receives a timely alert. Thus, geometries 4, 17, and 25 are potentially hazardous because their MIEVs are greater than TEL in Fig. 4, but they do not cause any integrity failure because those geometries are screened out by this VPL calculation and VAL comparison. However, if the airplane uses one of the other potentially hazardous geometries with indices 6, 7, 11, 12, 16, 21, and 26 with MIEVs exceeding TEL (Fig. 4) but whose VPLs are smaller than VAL (Fig. 5), those geometries will not be removed by the VPL calculation based on the nominal broadcast σ. If an airplane uses one of these geometries and, at the same time, the IPPs of the worst two satellites are impacted by an undetected large ionospheric gradient with the worst-case geometry as shown in Fig. 3, the position output of onboard avionics has unacceptable error but the pilot does not receive a timely alert. This would result in an integrity failure.

As explained in Sec. III.A, range-domain monitoring that relies upon the CCD monitor cannot meet the integrity requirement because ionospheric fronts are not observable to ionospheric-rate-based monitors under specific combinations of geometries (Fig. 3). Although some hazardous geometries are screened out by the nominal VPL calculation and VAL comparison, others will pass this test. Therefore, an additional defense is needed to protect against this possible integrity risk. The next section proposes a position-domain verification method to guarantee system integrity in the presence of ionospheric anomalies.

IV. Mitigating Ionospheric Threats by Position-Domain Geometry Screening

This section develops a position-domain geometry-screening method as a means to mitigate ionospheric threats. Because this method protects user integrity by indirectly removing or screening out potential user satellite geometries that would not be safe under the worst-case ionospheric anomaly, GBAS system availability is reduced. However, the results demonstrate that this method meets the integrity requirement with an acceptable loss of availability, especially when the realistic IEV equation defined here is applied to the position-domain screening algorithm.

A. Position-Domain Geometry Screening as a Means to Mitigate Ionospheric Threats

The key to screening out potentially hazardous satellite geometries is to selectively increase the integrity-related parameters broadcast by the ground facility. Among these parameters are the 1σ error bounds that contribute to the total user range-error variance σ_i^2 in Eqs. (5) and (6), which is decomposed as shown in Eqs. (7–9) (see Secs. 2.3.9.1, 2.3.12.1, and 2.3.12.3 in [8]):

$$\sigma_i^2 = \sigma_{\text{pr\_gnd},i}^2 + \sigma_{\text{tropo},i}^2 + \sigma_{\text{pr\_air},i}^2 + \sigma_{\text{iono},i}^2 \tag{7}$$

$$\sigma_{\text{pr\_air},i}^2 = \sigma_{\text{multipath},i}^2 + \sigma_{\text{noise},i}^2 \tag{8}$$

$$\sigma_{\text{iono},i} = F_i \sigma_{\text{vig}} (x_{\text{aircraft}} + 2\tau v_{\text{aircraft}}) \tag{9}$$

where σ_i^2 is the variance of a normal distribution that overbounds the true postcorrection range-domain error distribution for satellite i under the fault-free hypothesis, $\sigma_{\text{pr\_gnd},i}$ is the total fault-free 1σ ground error term associated with the corresponding differential correction error for satellite i, $\sigma_{\text{tropo,i}}$ is the 1σ ground error term associated with residual tropospheric uncertainty for satellite i, $\sigma_{\text{pr\_air},i}$ is the 1σ error term that bounds fault-free airborne receiver measurement error for satellite i, $\sigma_{\text{multipath},i}$ is the fault-free 1σ airborne error term associated with multipath error for satellite i, $\sigma_{\text{noise},i}$ is the fault-free 1σ airborne error term associated with receiver noise for satellite i, $\sigma_{\text{iono},i}$ is the 1σ ground error term associated with residual ionospheric uncertainty for satellite i, F_i is the vertical-to-slant ionospheric thin-shell-model obliquity factor (unitless) for satellite i, σ_{vig} is the standard deviation of a normal distribution associated with residual ionospheric uncertainty due to nominal spatial decorrelation (vig stands for vertical ionospheric gradient), x_{aircraft} is the horizontal separation between the GBAS ground facility and airplane, τ is the time constant of the single-frequency carrier-smoothing filter in the GBAS avionics, 100 s (same as that used in the ground facility), and v_{aircraft} is the horizontal-approach velocity of the airplane in the direction of the GBAS-equipped airport.

Recall that, as demonstrated in Figs. 4 and 5, the airborne VPL calculation in Eqs. (5) and (6) does not remove all potentially hazardous geometries if nominal σ are broadcast. However, if the GBAS ground facility increases the broadcast σ values or, in other words, inflates them above the nominal values, the airborne VPL increases as well. Once sufficient σ inflation is implemented, all hazardous geometries would be screened out because their individual VPLs would all exceed VAL. Of course, many geometries that are not hazardous will be screened out as well, leading to an unavoidable loss of availability.

A key design decision for geometry screening is to select the most effective parameter(s) to inflate among the broadcast σ. We selected σ_{vig} as the most effective parameter because increasing σ_{vig} naturally increases σ_i^2 in Eq. (7) as a function of the ground-to-aircraft separation x_{aircraft} [see Eq. (9)]. The inflated value of σ_{vig} (or, equivalently, the σ_{vig} inflation factor) should be just large enough to increase the VPL of all potentially hazardous geometries (recall that this means geometries with MIEVs exceeding TEL, as shown in Fig. 4) over VAL so that they cannot be used by airborne receivers. If the inflation factor is increased further, additional safe geometries will be screened out unnecessarily.

To obtain the minimum acceptable inflation factor, the ground facility calculates the MIEVs of all credible airborne subset geometries at a given epoch and then computes VPL for each of these geometries using the nominal $\sigma_{\text{vig}} = 4.0$ mm/km suggested in [14] and an initial (default) inflation factor $I_{\text{vig}} = 1$. In this paper, a more-conservative number, $\sigma_{\text{vig}} = 6.4$ mm/km, is used as the nominal value to include additional margin for anomalous tropospheric errors (this is in accordance with [19]). In general, VPLs for the all-in-view geometry and each credible airborne subset geometry are calculated using the inflated $\sigma_{\text{vig}} = 6.4 I_{\text{vig}}$ mm/km. If the VPLs computed using the initial (or current) value of σ_{vig} are not large enough to remove all potentially hazardous geometries, the ground facility increases the inflation factor I_{vig} by a small amount (we used a step size of 0.01) and performs the VPL calculations again using the updated inflation factor until all hazardous geometries are properly removed. After obtaining the minimum inflation factor that eliminates all hazardous geometries, the ground facility calculates and broadcasts the inflated σ_{vig} based on this inflation factor. Since the ground-facility processing involves position-domain calculation and verification (i.e., MIEV and VPL are calculated in the position domain and are compared with TEL and VAL, respectively), this method is called *position-domain geometry screening*. Note that, except for this procedure, the ground facility only implements range-domain (CCD) monitoring on a satellite-by-satellite basis. Although almost all other anomalies can be detected by the range-domain monitoring included in the category I GBAS ground facility, the worst-case ionospheric anomaly requires this additional mitigation technique.

Figure 6 illustrates geometry screening by σ_{vig} inflation using the same example satellite geometry shown in Figs. 4 and 5. After applying the inflated σ_{vig} values, the VPLs of the potentially hazardous geometries with MIEVs exceeding TEL (i.e., geometries 6, 7, 11, 12, 16, 21, 24, and 26) are now greater than VAL. Hence, all hazardous geometries are properly removed. The geometries 4, 17, and 25 are not displayed here because those geometries are already screened out without σ_{vig} inflation, as shown in Fig. 5. Unfortunately, the inflated σ_{vig} eliminates some safe geometries as well. For example, geometries 10, 15, 18, and 19 in Fig. 6 are safe to use because their MIEVs are smaller than TEL, but they are also removed from the approved set of geometries. This inevitable removal of safe geometries by σ_{vig} inflation reduces the availability of the GBAS system. The next section discusses the expected availability of GBAS-supported category I precision approach when the position-domain geometry-screening method is applied.

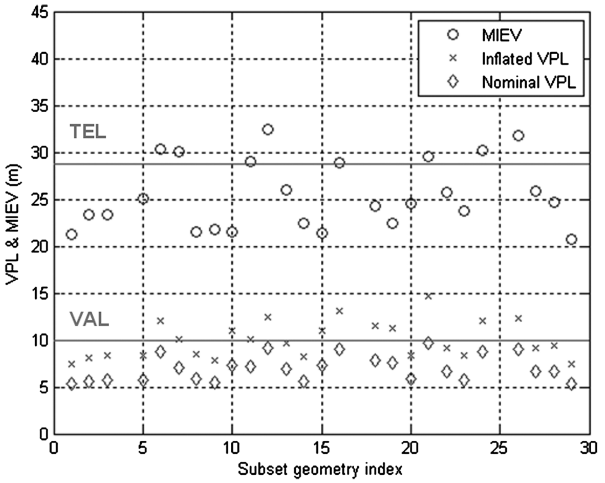

Fig. 6 Position-domain geometry screening by σ_{vig} inflation. (The inflation factor I_{vig} is 2.58 in this case.) The subset geometries with inflated VPLs exceeding VAL are not approved by airborne receivers. Hence, all hazardous geometries with MIEVs exceeding TEL are excluded after σ_{vig} inflation. The downside is that several safe geometries with MIEVs less than TEL are screened out as well. (An approaching airplane is assumed to be at 6 km from the ground facility in this simulation.)

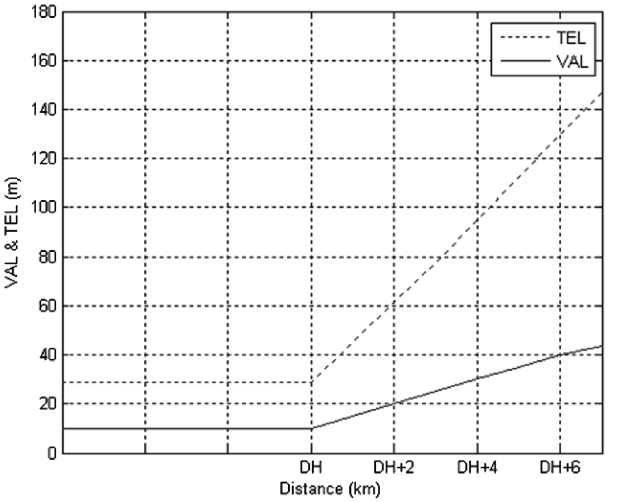

Fig. 7 TEL and VAL for category I precision approaches. Each runway has its own DH (distance from the ground facility to an airplane when the airplane reaches the minimum decision height of 200 ft).

B. Availability Analysis with Position-Domain Geometry Screening

Figure 6 illustrated an example result of position-domain geometry screening at a single epoch and a single distance from the ground facility that is at or near the maximum practical separation for existing airports. After applying the inflation factor to the VPL calculation, all potentially hazardous geometries at the given epoch and distance are screened out. To analyze the resulting system availability over a 24 h period of repeatable GPS satellite geometries, we calculate an inflation factor at every minute over 24 h (i.e., a total of 1440 epochs). In Fig. 6, we exclusively considered a distance of 6 km from the ground facility to an airplane that just reaches the 200 ft decision height (DH) of category I precision approaches (for simplicity, we notate this as DH = 6 km). However, DH can vary depending on the station and runway configuration. To cover all possible DHs, DH = 1 through 6 km (every 1 km) are considered in the simulation that generates inflation factors. In addition to the actual six DH distances, the simulation includes a hypothetical DH at 7 km to provide additional margin against granularity while protecting real DHs as far out as 6 km. The granularity problem comes from running simulations only for a limited number of discrete distances. As an example, the inflation factor required to protect a DH at 5.5 km could be larger than those driven by DH = 5 and 6 km. These small irregularities mean that the availability curve is not perfectly monotonic, but the curve as a whole decreases with increasing DH separation. Thus, a DH at 7 km generally requires more inflation than at 6 km, and adding it to the simulation provides margin against irregularities at shorter DH separations that are not sampled.

In addition to simulating a range of DH separations, an approaching airplane from DH + 7 km to the DH (checking every 1 km along this path) is simulated because the system must guarantee its integrity in this whole region. Consequently, a total of 56 cases (seven DHs and eight distances from a given DH) are considered at each epoch, and the largest inflation factor over all cases is chosen to obtain the new broadcast σ_{vig} of the epoch. The TELs [20] and VALs [8] at different distances from the DH location are shown in Fig. 7. Note that both TEL and VAL increase linearly beyond the DH because the distance from the nominal airplane path to potential obstacles grows.

For the availability analyses in this section, the standard RTCA 24-satellite GPS constellation (Table B-1 in [21]) is used, and the GBAS ground facility is assumed to be located at Newark airport (EWR) in New Jersey. The ground and airborne error models used in this study are plotted in Fig. 8. For the airborne error model, σ_{pr_air} in Eq. (8), the more-severe airborne error model is used for MIEV calculation (i.e., airborne noise model, σ_{noise}, with airborne accuracy designator A [8]), and the minimum error model (i.e., $\sigma_{noise} = 0$ or $\sigma_{pr\_air} = \sigma_{multipath}$) is used for VPL_{H0} and VPL_{eph} in Eqs. (5) and (6). This combination is a conservative choice because it maximizes MIEV while minimizing VPL. Thus, it considers more subset geometries as being potentially hazardous, and by increasing the gap between VPL and VAL, it increases the inflation factors required to remove potentially hazardous geometries. Separately, to determine the availability of the resulting VPL_{H0} and VPL_{eph} using inflated σ_{vig} (i.e., $I_{vig}\sigma_{vig}$), the less-severe error model (i.e., airborne noise model σ_{noise}, with airborne accuracy designator B [8]) is used to represent a more common state of airborne equipment.

With these settings, the required inflation factor I_{vig} at each epoch is calculated and shown in Fig. 9. It is notable that a significant fraction of epochs require no inflation; i.e., $I_{vig} = 1$ is sufficient. This tends to occur when the all-in-view geometry is very good such that all two-satellites-removed subsets are good enough to adequately resist the worst-case ionospheric anomaly. However, a substantial majority of epochs require inflation, and the amount of inflation often exceeds a factor of 2 and sometimes a factor of 3. This degree of σ_{vig} inflation may affect airborne user availability on some of these epochs. Note that an upper bound on I_{vig} exists because the maximum value of σ_{vig} that can be broadcast by GBAS is 25.5 mm/km [22].

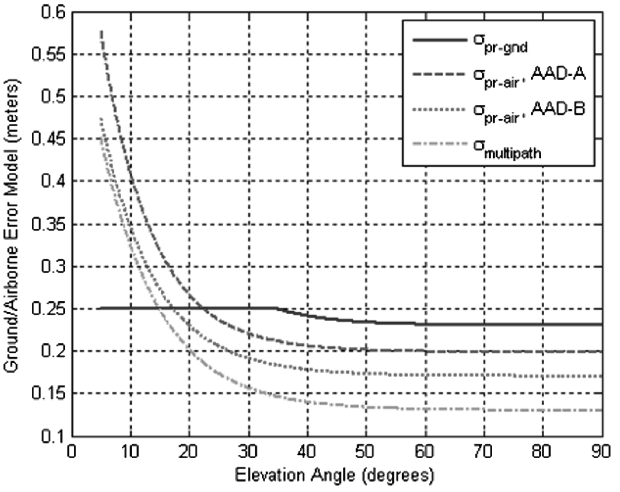

Fig. 8 Ground/airborne error models used in this paper; σ_{pr_gnd} (refer to [18,19]), σ_{pr_air} with airborne accuracy designator A (AAD-A), σ_{pr_air} with airborne accuracy designator B (AAD-B), and $\sigma_{multipath}$.

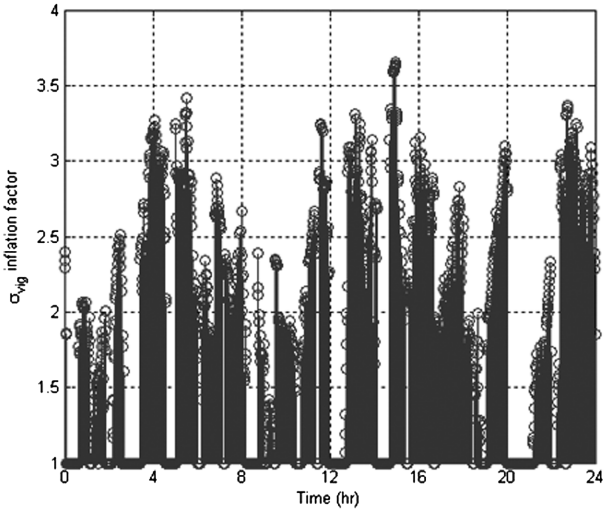

Fig. 9 The σ_{vig} inflation factors. The inflation factor at each epoch is the largest value among the inflation factors obtained at DH separations of 1 to 7 km (every 1 km) and aircraft distances from the DH of 0 to 7 km (every 1 km). The broadcast σ_{vig} is the nominal σ_{vig} of 6.4 mm/km times these inflation factors.

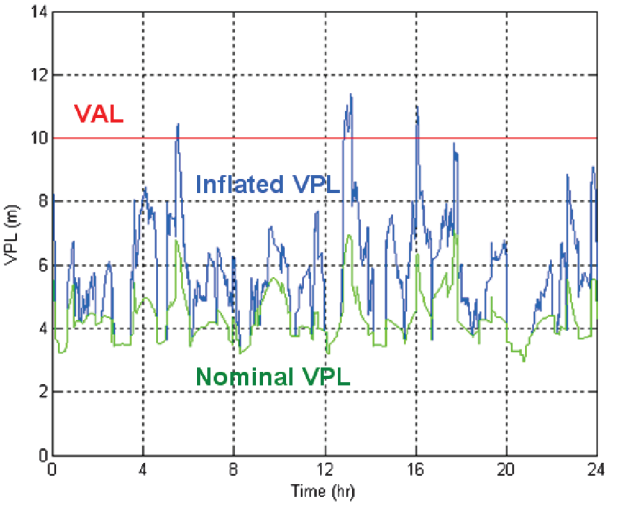

Fig. 10 Nominal VPL without inflation and inflated VPL (after applying the inflated σ_{vig}) at Newark airport. VPL at each epoch is the larger of VPL_{H0} in Eq. (5) and VPL_{eph} in Eq. (6). Availability during the 24 h period is 97.5% for a DH at 6 km and an aircraft using all satellites in view. The margin between VPL and VAL is significantly reduced after σ_{vig} inflation.

Given the nominal value of 6.4 mm/km used here, the maximum value of I_{vig} is $25.5/6.4 = 3.984$, or just under 4.0. The inflation factors for Newark in Fig. 9 stay within this constraint, but several epochs exceed 3.5 and thus come relatively close to it. If an inflation factor larger than this limit were ever required to protect integrity, the simplest option would be to discontinue the broadcast of differential corrections until the required inflation factor fell below the limit. Such a drastic step would not be needed if another broadcast parameter (such as σ_{pr_gnd}) could be inflated as well to exclude the potentially unsafe geometries that could not be removed by σ_{vig} at its maximum value.

By applying inflation factors to σ_{vig}, all potentially hazardous geometries (and many more acceptable geometries) are eliminated from the approved set of geometries. Hence, system integrity is guaranteed but with reduced system availability. We can estimate system availability at Newark for an aircraft at a DH 6 km from the ground facility using all satellites in view based on the VPL results in Fig. 10. In Fig. 10, nominal VPLs without inflation are always below the 10 m VAL at the DH. If VPL is lower than VAL at a particular epoch, the landing guidance service is available at the epoch (assuming that the aircraft uses all satellites in view, which it normally will). Hence, the availability during the 24 h period would have been 100% if the ionospheric anomaly threat did not exist or was less severe. Under the ionospheric threat model described earlier, the need for inflation of the broadcast σ_{vig} values results in VPLs that are also inflated, and there are several cases of VPLs exceeding VAL as shown in Fig. 10. The resulting availability impact is significant (97.5% availability instead of 100%), and the margin between VPL and VAL is reduced by inflation.

The degree of inflation required here is driven by the size of MIEV and the degree to which credible satellite subsets have MIEVs exceeding TEL. IEV for these results was determined by Eq. (4). This equation generates a conservative bound, but as will be explained shortly, it is too conservative to represent the threat model developed for CONUS. In the following section, we propose a modified equation for IEV to reduce the required inflation and improve availability without sacrificing integrity.

C. Availability Benefit from a More Realistic IEV Calculation

Equation (4) represents a very conservative expression to calculate IEV. As previously explained, this conservatism comes from considering all possible combinations of positive and negative differential range errors of two impacted satellites. If an anomalous gradient hits two satellites, as in Fig. 3, the pseudorange correction errors of both satellites induced by the same ionospheric gradient should have the same sign. It is not expected that the same ionospheric gradient causes a differential range delay for one satellite and a differential range advance on the other satellite. However, the carrier-smoothing filter [23] of GBAS avionics adds complexity to this picture. It is well known that the effects on code and carrier measurements due to dispersive media such as the ionosphere have the same magnitude but opposite signs, which means, for example, that positive code errors are accompanied by negative carrier errors. In GBAS, the carrier-smoothing filter smoothes code measurements with less-noisy carrier measurements using a 100 s time constant. Since carrier measurements dominate in the smoothing filter outputs shortly after the impact of an ionospheric gradient, the error of smoothed code during this initial response grows in the opposite direction with respect to the error from a converged filter [24]. Figure 11 illustrates this behavior. During the early phase of smoothing, the smoothed range error has a negative sign, but its magnitude, $c \cdot \varepsilon$ $(0 < c < 1)$, is much smaller than the positive magnitude of the maximum range error, ε $(0 < \varepsilon)$, of a converged filter (recall that ε can be obtained from Eqs. (1–3) depending on Δv of the corresponding satellite). For this reason, a positive range error of one satellite can be accompanied by a negative, but relatively small, range error of the other satellite when two satellites are impacted almost simultaneously by the same ionospheric gradient front.

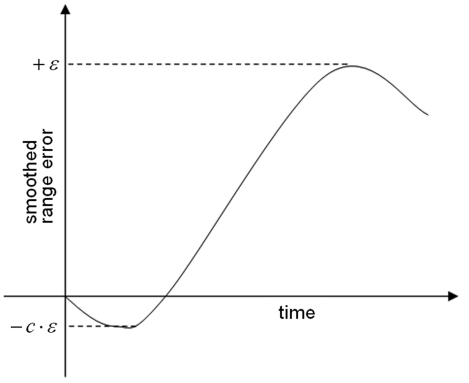

Fig. 11 Illustration of smoothed differential range error on a satellite after the impact of an ionospheric gradient. During the early phase of smoothing, the smoothed range error has a negative sign, although the smoothed range error from a converged filter has a positive sign in this example. Note that the magnitude of the maximum negative error, $c \cdot \varepsilon$, is much smaller than the magnitude of the maximum positive error, ε.

Although Eq. (4), which has been used in [18,19], covers the worst case of any possible combination of signs of differential range errors, it is a very conservative expression because it does not consider the characteristics of the carrier-smoothing filter described here and shown in Fig. 11. To represent the large magnitude difference between differential range errors with opposite signs of two impacted satellites, we suggest a more realistic expression to calculate IEV in Eq. (10):

$$\mathrm{IEV}_{k1,k2} = \max\{|S_{\mathrm{vert},k1}\varepsilon_{k1} + S_{\mathrm{vert},k2}\varepsilon_{k2}|, |S_{\mathrm{vert},k1}\varepsilon_{k1} - c \cdot S_{\mathrm{vert},k2}\varepsilon_{k2}|, |S_{\mathrm{vert},k2}\varepsilon_{k2} - c \cdot S_{\mathrm{vert},k1}\varepsilon_{k1}|\} \quad (10)$$

The first term, $|S_{\mathrm{vert},k1}\varepsilon_{k1} + S_{\mathrm{vert},k2}\varepsilon_{k2}|$, represents the larger vertical error between a positive-positive range-error combination of two impacted satellites (i.e., $S_{\mathrm{vert},k1}\varepsilon_{k1} + S_{\mathrm{vert},k2}\varepsilon_{k2}$) and a negative-negative range-error combination (i.e., $-S_{\mathrm{vert},k1}\varepsilon_{k1} - S_{\mathrm{vert},k2}\varepsilon_{k2}$) because

$$\max\{S_{\mathrm{vert},k1}\varepsilon_{k1} + S_{\mathrm{vert},k2}\varepsilon_{k2}, -S_{\mathrm{vert},k1}\varepsilon_{k1} - S_{\mathrm{vert},k2}\varepsilon_{k2}\} = |S_{\mathrm{vert},k1}\varepsilon_{k1} + S_{\mathrm{vert},k2}\varepsilon_{k2}| \quad (11)$$

Similarly, the second and the third terms of Eq. (10) consider positive-negative range-error combinations. To represent the constraint shown above, once one satellite has a range error of ε_{k1}, the other satellite can only have a range error of $-c \cdot \varepsilon_{k2}$, which cannot be greater than $-\varepsilon_{k2}$ in magnitude. The maximum of these three terms in Eq. (10) is the largest possible IEV under any combination of signs of range errors between two satellites impacted by the same ionospheric gradient, as in Fig. 3.

If the c factor in Fig. 11 and Eq. (10) is assumed to be 1, the realistic IEV equation in Eq. (10) becomes the same as the conservative IEV equation in Eq. (4) (see the Appendix for proof). Therefore, Eq. (4) is merely the most conservative case of Eq. (10) when we consider the unrealistic situation of equally large positive and negative range errors (i.e., ε_{k1} and $-\varepsilon_{k2}$) on two impacted satellites. It is emphasized again that combinations of ε_{k1} and ε_{k2} or $-\varepsilon_{k1}$ and $-\varepsilon_{k2}$ of two impacted satellites are realistic, but combinations of ε_{k1} and $-\varepsilon_{k2}$, or $-\varepsilon_{k1}$ and ε_{k2} are not realistic. Only ε_{k1} and $-c \cdot \varepsilon_{k2}$, or $-c \cdot \varepsilon_{k1}$ and ε_{k2} with $0 < c < 1$ are realistic if the range errors of two satellites have opposite signs. Luo et al. [24] showed that the magnitude of differential range errors during the early phase of smoothing is less than 20% of the magnitude of differential range errors from a converged filter. Hence, $c = 0.2$ provides a reasonable bound on the differential range errors with opposite signs when two satellites are impacted by the same ionospheric gradient.

Note that the discussion thus far pertains to two satellites impacted by the same ionospheric gradient. However, the filament structure of enhanced ionospheric delay observed in CONUS on 20 November 2003 (as shown in Fig. 12) indicates a possible exception. In this situation, it is possible for one affected satellite to observe a positive change in delay from the increasing-delay gradient that forms the leading edge of the filament, while another satellite simultaneously observes a negative change in delay from the decreasing-delay gradient that forms the trailing edge. In other words, under very rare circumstances, two satellites can be impacted by two different ionospheric gradients having opposite signs. However, the worst-case gradient would not be present on both edges at the same time. All of the near-maximum-gradient observations made from this event (for both high- and low-elevation satellites) came from the trailing edge at the time when the sharp downward change was observed in Ohio (just after 21:00 UT on 20 November 2003). The gradient on the leading edge ranged from roughly 30 to 120 mm/km, which is much lower than the (up to) 425 mm/km seen at the worst place and time on the trailing edge (Fig. 10 of [6]). Therefore, even this case better fits the proposed realistic IEV equation than the conservative IEV equation. The only change would be that the c factor in Eq. (10) might have to be increased from 0.2. If we take the ratio of 120/425 as a guideline, c would increase to about 0.28, and $c = 0.5$ would be a very conservative bound on this dual-front scenario.

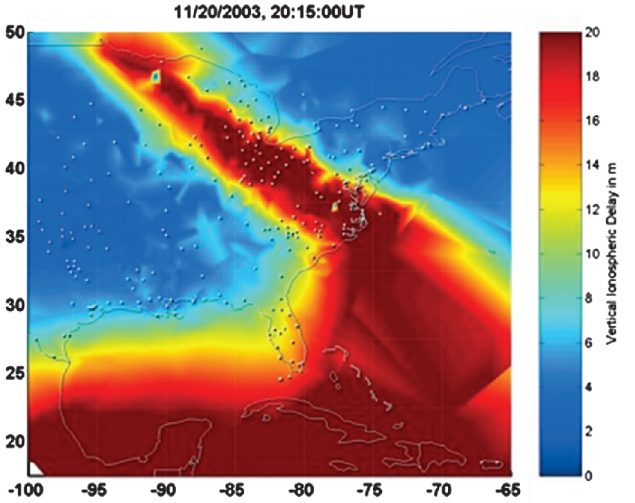

Fig. 12 Map of vertical ionospheric delay over eastern United States on 20 November 2003 at 20:15 UT (reproduction of Fig. 2 of [6]).

The benefit of the realistic IEV equation in Eq. (10) is clearly shown in Fig. 13. Comparing with Fig. 6, The MIEVs of the subset geometries are significantly reduced by the realistic IEV equation with $c = 0.5$. As a result, only one geometry (i.e., geometry 12) with MIEV exceeding TEL but VPL lower than VAL is potentially hazardous. (Remember that eight geometries are potentially hazardous in Fig. 6 applying the conservative IEV equation.) Thus, small inflation with $I_{\mathrm{vig}} = 1.47$ is enough to screen the potentially hazardous geometry. By this inflation, two safe geometries (i.e., geometries 16 and 21) are also screened, but the number of approved geometries in Fig. 13 is 23, which is significantly better than the 14 approved geometries after the geometry screening in Fig. 6. The reduced inflation of VPL is directly related to availability benefit.

Using the realistic IEV equation proposed in Eq. (10), the availability analysis of the position-domain geometry-screening method is performed again. For this analysis, the cases of $c = 0.2$ and 0.5 are evaluated and compared. As shown in Fig. 14, the inflated VPLs with the realistic IEV calculation are not much greater than the nominal VPLs without σ_{vig} inflation, and 100% availability for aircraft using all satellites in view is achievable in these cases at Newark airport. More important, the new IEV equation provides significant margin between the inflated VPLs and VAL for both $c = 0.2$ and 0.5, which is a major improvement compared with Fig. 10. Very similar results were obtained for Memphis airport (MEM), as shown in Fig. 15. Therefore, the position-domain

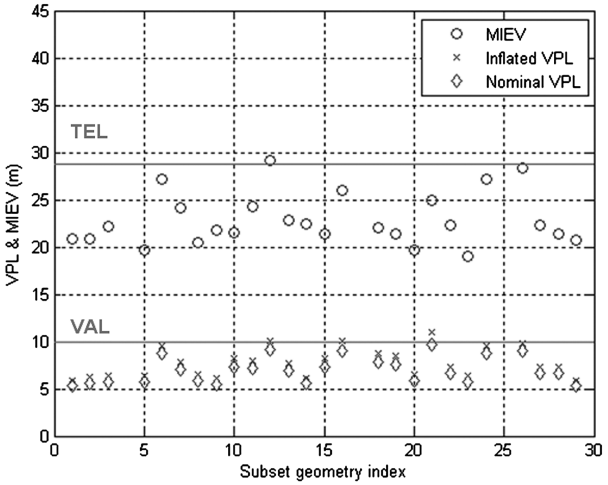

Fig. 13 Reduced MIEVs due to the realistic IEV equation with $c = 0.5$. (Except for the IEV equation, all other settings are the same as Fig. 6.) Comparing with Fig. 6, the inflation factor I_{vig} is significantly reduced from 2.58 to 1.47.

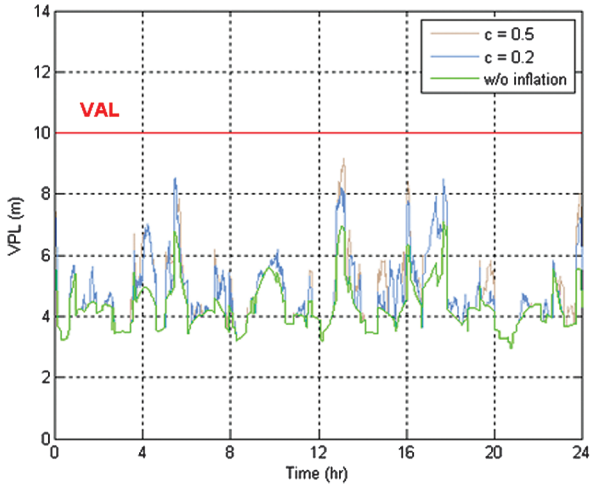

Fig. 14 Inflated VPLs calculated using the realistic IEV equation with $c = 0.2$ and $c = 0.5$ at Newark airport. $c = 0.2$ is a conservative value for two satellites impacted by a single ionospheric gradient, while $c = 0.5$ is a very conservative value that bounds all observed anomalous ionospheric conditions in CONUS, including a case where two gradients were caused by the same anomaly. For both cases, the gap between the inflated VPL and VAL is much larger than in Fig. 10.

geometry-screening method proposed in this paper can mitigate the worst-case ionospheric anomalies with a tolerable sacrifice of availability, especially when the newly proposed IEV equation is applied.

V. Real-Time Implementation of Geometry Screening

To be useful for ionospheric threat mitigation, the algorithms described in this paper must operate in real time within GBAS ground stations. It is theoretically possible to determine a worst-case inflation factor for a particular location via offline simulation, but it would be difficult to bound the set of possible variations of the GPS satellite constellation. Any reasonable allowance for significant constellation variation would likely create cases where the inflation factor exceeds the maximum allowed broadcast value of 3.984 derived in Sec. IV.B. Even if the maximum inflation factor in Fig. 9 (about 3.7) were accepted as the maximum possible value and were used all the time, the resulting category I approach availability would be unacceptably poor.

Because the simulation of all possible subset geometries to determine MIEV and the resulting inflation-factor search cannot be performed at the same rate that type I GBAS messages are updated (twice per second), a slower update rate that corresponds to the rate of change of GPS satellite geometries must be selected. After some investigation, an inflation-factor update interval of 1 min (60 s, or 120 epochs at 2 Hz) has proven to be workable. Note that, if 1 min updates are used, a new inflation factor must be valid for the 60 s interval going forward until it is updated. In other words, when the geometry-screening algorithm determines a new inflation factor to be broadcast from time t_1, that inflation factor must be valid over the interval $[t_1, t_1 + 60\text{ s}]$. Therefore, separate inflation factors must be computed in advance for t_1 and $(t_1 + 60\text{ s})$, and the larger of the two resulting inflation factors becomes the one that is broadcast over this interval.

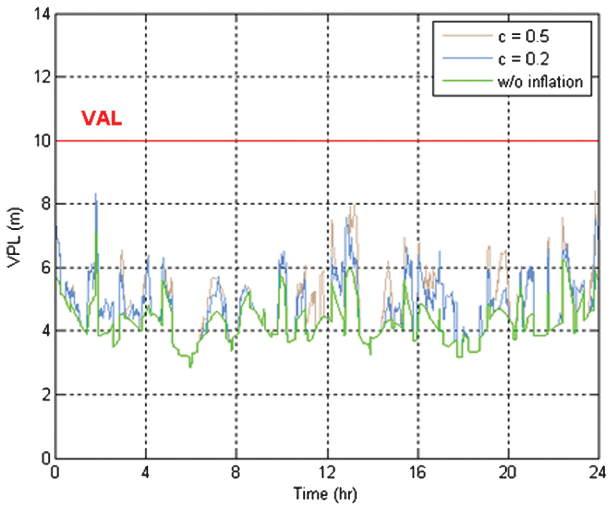

Fig. 15 Inflated VPLs calculated using the realistic IEV equation with $c = 0.2$ and 0.5 at Memphis airport. This result is very similar to the case of Newark in Fig. 14.

Recall that the only thing that changes over time is the visible GPS satellite geometry. The procedure outlined above assumes that the 60 s update interval is short enough compared with the change in satellite geometry that the maximum of the t_1 and $(t_1 + 60\text{ s})$ inflation factors is an acceptable bound on the entire interval. This assumption is clearly not perfect, but the error in it is acceptable as long as the interval between inflation-factor updates is reasonably short. Shorter intervals also have the effect of reducing the slight availability loss that comes from taking the maximum of two inflation factors over the update interval.

Regardless of the update interval chosen, a special procedure has to be added to handle sudden, unexpected losses of visible satellites in between normal inflation-factor updates. A sudden satellite loss can significantly increase the required inflation factor, but the ground-screening algorithms cannot be rerun to generate updated numbers instantly. Several strategies exist to handle this situation. The simplest is to delay updating as long as the ground-system time-to-alert allocation allows (3 s for category I precision approach). If a new inflation factor is not ready at that point, the maximum value of σ_{vig} (25.5 mm/km) can be broadcast until it is ready. This approach is nonoptimal in that it increases continuity risk more than is necessary. Alternatives that include precalculating inflation factors that would apply in case of satellite loss within the next update interval are preferable if computational resources allow this to be done within acceptably short update intervals.

Because GBAS ground stations do not interact with the outside world, they currently have no means of distinguishing anomalous ionospheric conditions beyond the monitors mentioned in this paper. The presence of potential ionospheric threats must be presumed at all times; therefore, geometry screening must be active at all times. This is very costly, as precision-approach availability is always sacrificed even though it is very rare for the ionosphere to be anomalous enough to potentially threaten GBAS. Furthermore, because geometry screening is not sufficient to support the GBAS Differentially Corrected Positioning Service (DCPS), DCPS has not yet been approved for use [19].

Several alternatives that would provide GBAS with sufficient knowledge to discontinue geometry screening and σ_{vig} inflation when the ionosphere is known to be nonthreatening have been proposed. One is to allow GBAS stations within good Satellite-Based Augmentation System (SBAS) coverage to use SBAS ionospheric corrections and error bounds as a means of determining when the ionosphere is nonthreatening [25]. This method is the easiest to integrate into GBAS since SBAS correction messages are broadcast as GPS L1 C/A-code signals. Whereas the benefits of SBAS information would be limited to regions with good SBAS coverage, SBAS is expected to expand to cover a large majority of the populated world over the next decade. Another approach that would require a new data channel into GBAS would be the use of improved space weather forecasts and to alert GBAS stations of the potential for ionospheric anomalies. A great deal of progress has been made in space weather forecasting and nowcasting over the past decade, but unlike SBAS, the current state of the art appears to fall short of the level of assurance needed for use in safety-critical systems.

VI. Conclusions

Anomalous ionospheric gradients that have been observed during severe ionospheric storms pose a potential integrity threat to

GNSS-based aircraft landing guidance systems. Under worst-case gradient configurations and aircraft approach geometries, anomalous gradients cannot be detected by the code-minus-carrier (CCD) range-domain monitor within a GBAS ground facility. Undetected gradients can cause unacceptable range errors for certain satellite geometries that can possibly be used by an approaching airplane. For category I precision-approach operations, it is not practical to modify airborne equipment that has already been certified. Instead, this paper proposes a method for position-domain threat evaluation and geometry screening performed by the GBAS ground facility. Once values of σ_{vig} inflated as needed by the position-domain screening process are broadcast, all potentially hazardous geometries with large undetected range errors are eliminated from the set of geometries that can be approved by the VPL calculation onboard the aircraft. This position-domain screening process requires significant software changes to the ground facility but does not require any modifications to airborne equipment or to the ground-to-airborne interface definition. However, the availability of the landing guidance system is reduced after the airborne VPL is inflated by the screening process.

To minimize the availability impact of geometry screening, this paper proposes a modified equation for worst-case ionospheric error impacts that removes unnecessary conservatism from previous calculations. Using this revised algorithm, availability analyses demonstrated that better than 99.9% availability for category I precision approach is attainable with margin at both Newark and Memphis airports without compromising system integrity.

The GAST-D upgrade to GBAS to support category II and III operations will make use of the lessons learned in developing geometry screening for category I ground systems. Monitoring will be added to both ground systems and avionics such that ground-based geometry screening is no longer necessary. Instead, each aircraft will perform its own screening based upon knowledge of its particular preapproach satellite geometry and its specific performance characteristics.

Appendix: Proof of IEV Equivalence When $c = 1$

This Appendix proves Eq. (A1), which states that Eq. (10) is the same as Eq. (4) when $c = 1$:

$$\max\{|S_{\text{vert},k1}\varepsilon_{k1} + S_{\text{vert},k2}\varepsilon_{k2}|, |S_{\text{vert},k1}\varepsilon_{k1} - S_{\text{vert},k2}\varepsilon_{k2}|\} = |S_{\text{vert},k1}\varepsilon_{k1}| + |S_{\text{vert},k2}\varepsilon_{k2}| \tag{A1}$$

Since the left-hand side and the right-hand side of Eq. (A1) are all positive, Eq. (A1) is equivalent to Eq. (A2):

$$\max\{(S_{\text{vert},k1}\varepsilon_{k1} + S_{\text{vert},k2}\varepsilon_{k2})^2, (S_{\text{vert},k1}\varepsilon_{k1} - S_{\text{vert},k2}\varepsilon_{k2})^2\} = (|S_{\text{vert},k1}\varepsilon_{k1}| + |S_{\text{vert},k2}\varepsilon_{k2}|)^2 \tag{A2}$$

The left-hand side of Eq. (A2) can be expanded as follows:

$$\begin{aligned}&\max\{(S_{\text{vert},k1}\varepsilon_{k1} + S_{\text{vert},k2}\varepsilon_{k2})^2, (S_{\text{vert},k1}\varepsilon_{k1} - S_{\text{vert},k2}\varepsilon_{k2})^2\}\\ &= \max\{S^2_{\text{vert},k1}\varepsilon^2_{k1} + S^2_{\text{vert},k2}\varepsilon^2_{k2} + 2\\ &\cdot S_{\text{vert},k1}\varepsilon_{k1}S_{\text{vert},k2}\varepsilon_{k2}, S^2_{\text{vert},k1}\varepsilon^2_{k1} + S^2_{\text{vert},k2}\varepsilon^2_{k2} - 2\\ &\cdot S_{\text{vert},k1}\varepsilon_{k1}S_{\text{vert},k2}\varepsilon_{k2}\} = S^2_{\text{vert},k1}\varepsilon^2_{k1} + S^2_{\text{vert},k2}\varepsilon^2_{k2}\\ &+ \max\{2\cdot S_{\text{vert},k1}\varepsilon_{k1}S_{\text{vert},k2}\varepsilon_{k2}, -2\cdot S_{\text{vert},k1}\varepsilon_{k1}S_{\text{vert},k2}\varepsilon_{k2}\}\end{aligned} \tag{A3}$$

The right-hand side of Eq. (A2) can be similarly expanded as follows:

$$(|S_{\text{vert},k1}\varepsilon_{k1}| + |S_{\text{vert},k2}\varepsilon_{k2}|)^2 = S^2_{\text{vert},k1}\varepsilon^2_{k1} + S^2_{\text{vert},k2}\varepsilon^2_{k2} + 2|S_{\text{vert},k1}\varepsilon_{k1}S_{\text{vert},k2}\varepsilon_{k2}| \tag{A4}$$

Since the first term in Eq. (A3) also appears in Eq. (A4), we only need prove Eq. (A5) to show that Eqs. (A3) and (A4) are the same:

$$\max\{2\cdot S_{\text{vert},k1}\varepsilon_{k1}S_{\text{vert},k2}\varepsilon_{k2}, -2\cdot S_{\text{vert},k1}\varepsilon_{k1}S_{\text{vert},k2}\varepsilon_{k2}\} = 2|S_{\text{vert},k1}\varepsilon_{k1}S_{\text{vert},k2}\varepsilon_{k2}| \tag{A5}$$

Since $\max\{a, -a\} = |a|$ for any real number a, Eq. (A5) is true. Therefore, Eq. (A2) is proven; thus Eq. (A1) is also proven.

Acknowledgments

The authors would like to thank Ming Luo at Stanford University; Mats Brenner at Honeywell; and John Warburton, Tom Dehel, Bruce DeCleene, Barbara Clark, and Jason Burns of the Federal Aviation Administration (FAA) for their help and support of this research. We also would like to express special thanks to Attila Komjathy of the NASA Jet Propulsion Laboratory for providing us with data and comments. Funding support from the FAA Satellite Navigation Local Area Augmentation System Program Office is greatly appreciated. However, the opinions discussed in this paper are those of the authors and do not necessarily represent those of the FAA or other agencies.

References

[1] Enge, P., "Local Area Augmentation of GPS for the Precision Approach of Aircraft," *Proceedings of the IEEE*, Vol. 87, No. 1, Jan. 1999, pp. 111–132. doi:10.1109/5.736345

[2] Misra, P., and Enge, P., *Global Positioning System: Signals, Measurement, and Performance*, 2nd ed., Ganga-Jamuna, Lincoln, MA, 2006.

[3] Kaplan, E. D., and Hegarty, C. J. (eds.), *Understanding GPS: Principles and Applications*, 2nd ed., Artech House, Norwood, MA, 2006.

[4] Datta-Barua, S., Walter, T., Pullen, S., Luo, M., Blanch, J., and Enge, P., "Using WAAS Ionospheric Data to Estimate LAAS Short Baseline Gradients," *Proceedings of the 2002 National Technical Meeting of the Institute of Navigation*, San Diego, CA, Jan. 2002, pp. 523–530.

[5] Enge, P., Walter, T., Pullen, S., Kee, C., Chao, Y.-C., and Tsai, Y.-J., "Wide Area Augmentation of the Global Positioning System," *Proceedings of the IEEE*, Vol. 84, No. 8, Aug. 1996, pp. 1063–1088. doi:10.1109/5.533954

[6] Datta-Barua, S., Lee, J., Pullen, S., Luo, M., Ene, A., Qiu, D., Zhang, G., and Enge, P., "Ionospheric Threat Parameterization for Local Area Global-Positioning-System-Based Aircraft Landing Systems," *Journal of Aircraft*, Vol. 47, No. 4, July 2010, pp. 1141–1151. doi:10.2514/1.46719

[7] Ene, A., Qiu, D., Luo, M., Pullen, S., and Enge, P., "A Comprehensive Ionosphere Storm Data Analysis Method to Support LAAS Threat Model Development," *Proceedings of the 2005 National Technical Meeting of the Institute of Navigation*, San Diego, CA, Jan. 2005, pp. 110–130.

[8] *Minimum Operational Performance Standards for GPS Local Area Augmentation System Airborne Equipment*, RTCA, Rept. DO-253C, Washington, D.C., Dec. 2008.

[9] Mayer, C., Belabbas, B., Jakowski, N., Meurer, M., and Dunkel, W., "Ionosphere Threat Space Model Assessment for GBAS," *Proceedings of the 22nd International Technical Meeting of the Satellite Division of the Institute of Navigation*, Savannah, GA, Sept. 2009, pp. 1091–1099.

[10] Lee, J., Luo, M., Pullen, S., Park, Y. S., Enge, P., and Brenner, M., "Position-Domain Geometry Screening to Maximize LAAS Availability in the Presence of Ionosphere Anomalies," *Proceedings of the 19th International Technical Meeting of the Satellite Division of the Institute of Navigation*, Fort Worth, TX, Sept. 2006, pp. 393–408.

[11] Jensen, D., "SLS-4000 GBAS—The Future is Near," *7th International GBAS Working Group Meeting (I-GWG-7)*, Rio de Janeiro, Brazil, April 2008.

[12] Braff, R., and Shively, C., "A Method of Over Bounding Ground Based Augmentation System (GBAS) Heavy Tail Error Distributions," *Journal of Navigation*, Vol. 58, No. 1, Jan. 2005, pp. 83–103. doi:10.1017/S0373463304003029

[13] Harris, M., and Murphy, T., "Geometry Screening for GBAS to Meet CAT III Integrity and Continuity Requirements," *Proceedings of the 2007 National Technical Meeting of the Institute of Navigation*, San Diego, CA, Jan. 2007, pp. 1221–1233.

[14] Lee, J., Pullen, S., Datta-Barua, S., and Enge, P., "Assessment of Ionosphere Spatial Decorrelation for Global Positioning System-Based Aircraft Landing Systems," *Journal of Aircraft*, Vol. 44, No. 5, 2007, pp. 1662–1669. doi:10.2514/1.28199

[15] Khanafseh, S., Yang, F., Pervan, B., Pullen, S., and Warburton, J., "Carrier Phase Ionospheric Gradient Ground Monitor for GBAS with Experimental Validation," *Proceedings of the 23rd International*

Technical Meeting of the Satellite Division of the Institute of Navigation, Portland, OR, Sept. 2010, pp. 2603–2610.

[16] Simili, D. V., and Pervan, B., "Code-Carrier Divergence Monitoring for the GPS Local Area Augmentation System," *Proceedings of the IEEE/ION Position, Location, and Navigation Symposium 2006*, San Diego, CA, Apr. 2006, pp. 483–493.

[17] Ramakrishnan, S., Lee, J., Pullen, S., and Enge, P., "Targeted Ephemeris Decorrelation Parameter Inflation for Improved LAAS Availability During Severe Ionosphere Anomalies," *Proceedings of the 2008 National Technical Meeting of the Institute of Navigation*, San Diego, CA, Jan. 2008, pp. 354–366.

[18] Park, Y. S., Pullen, S., and Enge, P., "Enabling LAAS Airport Surface Movement: Mitigating the Anomalous Ionospheric Threat," *Proceedings of the IEEE/ION Position, Location, and Navigation Symposium 2010*, Indian Wells, CA, May. 2010, pp. 667–679.

[19] Murphy, T., Harris, M., Park, Y. S., and Pullen, S., "GBAS Differentially Corrected Positioning Service Ionospheric Anomaly Errors Evaluated in an Operational Context," *Proceedings of the 2010 International Technical Meeting of the Institute of Navigation*, San Diego, CA, Jan. 2010, pp. 394–410.

[20] Shively, C. A., and Niles, R., "Safety Concepts for Mitigation of Ionospheric Anomaly Errors in GBAS," *Proceedings of the 2008 National Technical Meeting of the Institute of Navigation*, San Diego, CA, Jan. 2008, pp. 367–381.

[21] *Minimum Operational Performance Standards for Global Positioning System/Wide Area Augmentation System Airborne Equipment*, RTCA, Rept. DO-229D, Washington, D. C., Dec. 13, 2006.

[22] *GNSS-Based Precision Approach Local Area Augmentation System (LAAS) Signal-in-Space Interface Control Document*, RTCA, Rept. DO-246D, Washington, D. C., Dec. 16, 2008.

[23] Hatch, R., "The Synergism of GPS Code and Carrier Measurements," *Proceedings of the 3rd International Geodetic Symposium on Satellite Doppler Positioning*, 1982, pp. 1213–1231.

[24] Luo, M., Pullen, S., Akos, D., Xie, G., Datta-Barua, S., Walter, T., and Enge, P., "Assessment of Ionospheric Impact on LAAS Using WAAS Supertruth Data," *Proceedings of the 58th Annual Meeting of the Institute of Navigation and CIGTF 21st Guidance Test Symposium*, Albuquerque, NM, Jun. 2002, pp. 175–186.

[25] Pullen, S., Luo, M., Walter, T., and Enge, P., "Using SBAS to Enhance GBAS User Availability: Results and Extensions to Enhance Air Traffic Management," *Proceedings of the 2nd ENRI International Workshop on ATM/CNS (EIWAC 2010)*, Tokyo, Nov. 2010.